RESEARCH ARTICLE OPEN ACCESS

Enhanced Catalytic Performance via Ultrasonication-Plasma Synergy in PtGaPCoO$_X$ Catalysts Under Mild Conditions

Wail Al Zoubi[1] 🄳 | Yujun Sheng[1] | Mohammad R. Thalji[2] | Bassem Assfour[3] | Stefano Leoni[4] | Abdullah Al Mahmud[5] | Jee-Hyun Kang[6] | Abdul Wahab Allaf[3,7] | Young Gun Ko[1]

[1]Integrated Materials Chemistry Laboratory, School of Materials Science and Engineering, Yeungnam University, Gyeongsan, Republic of Korea | [2]Korea Institute of Energy Technology (KENTECH), 21 KENTECH-gil, Naju, Jeollanam-do, Republic of Korea | [3]Department of Chemistry, Atomic Energy Commission, Damascus, Syria | [4]Cardiff University School of Chemistry, Cardiff, UK | [5]School of Chemical Engineering, Yeungnam University, Gyeongsan, Republic of Korea | [6]School of Materials Science and Engineering, Institute of Materials Technology, Yeungnam University, Gyeongsan, Republic of Korea | [7]Department of Pharmaceutical Chemistry and Quality Control. Faculty of Pharmacy, Arab International University, Damascus, Syria

Correspondence: Wail Al Zoubi (wailalzoubi@ynu.ac.kr)

ABSTRACT

The synergistic effect of bi-component support catalysts via facile synthesis remains a pivotal challenge in catalysis, particularly under mild conditions. Therefore, this study reports an ultrasonication-plasma strategy to produce a PtGaPCoCoO@TiO$_x$ site catalyst encapsulated within a high-entropy alloy framework. This approach harnesses instantaneous high-temperature plasma generated using an electrical field and ultrasonication under ambient conditions in H$_2$O. This study also elucidates the origin of the bifunctional effect in high-loading, ultra-stable, and ultra-fine PtGaPCoCoO catalysts, which are coated with a reducible TiO$_x$ layer, thereby achieving optimal catalytic activity and hydrogen evolution reaction (HER) performance. PtGaPCo intimacy in PtGaPCoCoO@TiO$_x$ is tuned and distributed on the porous titania coating based on strong metal–support interactions by leveraging the instantaneous high-energy input from plasma discharge and ultrasonication under ambient conditions in H$_2$O. PtGaPCoCoO@TiO$_x$ exhibits remarkable selectivity and durability in the hydrogenation of 3-nitrophenylacetylene, even after 25 cycles with high conversion rates, significantly outperforming comparative catalysts lacking the ultrasonication plasma treatment and other reported catalysts. Furthermore, the catalyst exhibits exceptional HER activity, demonstrated by an overpotential of 187 mV at a current density of 10 mA cm^{-2} and a Tafel slope of 152 mV dec^{-1}. This enhancement can be attributed to an increased electron density on the Pt surface within the PtGaPCo alloy. These findings highlight the potential of achieving synergistic chemical interactions among active metal sites in stable, industry-applicable catalysts.

1 | Introduction

Bi-component nanoparticles (NPs), heralded for their catalytic, electronic, optical, and magnetic properties superior to those of their individual components, have garnered significant interest. This is attributed to the intimate contact between disparate components, a phenomenon understood as a bifunctional or synergistic effect. However, comprehending and synthesizing these bifunctional effects[1]–whether through short- or long-range interactions and identifying active sites present considerable challenges. These challenges stem from the nuanced tuning of bi-component intimacy and the limitations inherent in traditional methods for controlling the microstructures [1]. Thus, pursuing a comprehensive and effective strategy for fabricating TiO_2-supported PtGaPCoCoO catalysts, notable for their high stability and superior activity, remains a central research challenge.

Bimetallic catalysts should exhibit proximity to optimize catalysis, fostering enhanced electron-interface interactions. However, the dynamics of metal–metal and metal–metal oxide interactions complicate the identification of catalytically active sites due to the multiplicity of such sites under reaction conditions. Recent studies have explored the impact of intimacy on catalyst activity, adjusting bimetals across nanoscale to millimeter scale distances [2–4]. Phaahlamohlaka et al. reported the effect of hydrogen spillover in Co catalysts in Fischer–Tropsch synthesis (FTS) using mesoporous hollow carbon spheres as a physical barrier in the presence of initiator Ru NPs and Co_3O_4 as an acceptor, which was loaded onto the support via conventional incipient wetness impregnation.[4] Karim et al. placed controlled iron oxide (FeO_x) and Pt NPs at nanoscale distances on reducible TiO_2 and nonreducible Al_2O_3 supports using the enhanced precision of top-down nanofabrication, and investigated the spatial extent of hydrogen spillover on both reducible and nondeducible supports [5]. Li et al. described isolated Pd atoms supported over indium oxide ((Pd_1/In_2O_{3-x})), in which the Pd atoms coordinated with four adjacent neighboring oxygen atoms to form a Lewis acid-base pair, achieving excellent catalytic performance in the hydrogenation of nitrobenzene to aniline [6]. Wu et al. reported the effect of subsurface composition on supported core-shell NPs (Pt_3Mn shell on Pt core) using a sequential incipient wetness impregnation method [7]. A Pt_3Mn subsurface exhibited high activity during propane dehydrogenation at 550°C, owing to low hydrogen adsorption and enhanced C-H activation selectivity.

Cai et al. prepared Pt-3dTM (3dTM: 3d transition metal) (M = Co, Fe, Ni) bimetallic catalysts using a wetness impregnation method with post-acid leaching treatments [8–10]. Overall, the current bicomponent catalytic systems face several challenges. The synthesis strategies of metal oxide-supported bicomponent catalytic systems are rather complex or not common approaches, the chemical structural information on metal oxide-supported bicomponent catalysts has not been profoundly discovered, the potential catalytic performance of bicomponent catalysts has not been appropriately explored, and the complicated catalytic mechanism of bicomponent catalysts has not been elucidated. Hence, the rational design of metal-oxide-supported bi-component catalytic systems is critically needed. Such advancement would elevate bi-component catalysts to the forefront of catalytic research and accelerate progress across the catalysis domain.
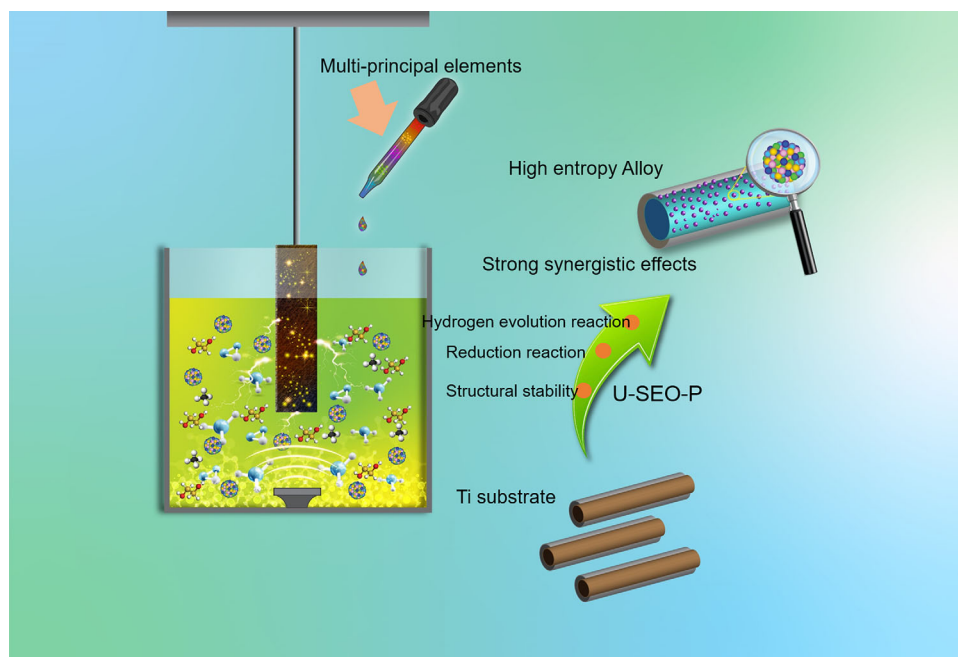
One-pot ultrasonic-assisted coincided electro-oxidation–reduction-precipitation (U-SEO-P) is the first technique to emerge as a potent method for fabricating highly dispersed ultra-small high-entropy alloy (us-HEA) NPs and conformal thin films on a Ti platform, as shown in Scheme 1. The us-HEA (PtGaPCoCoO) NPs demonstrate a uniform distribution across the reducible TiO_2 supports, boasting an average particle size of 2 nm, the smallest recorded among the studied HEAs.

High-angle annular dark-field scanning transmission electron microscopy (HAADF-STEM) and high-resolution transmission electron microscopy (HR-TEM) imaging measurements reveal the electronic structure, atomic structure, and coordination structure of us-HEA. In PtGaPCoCoCoO, PtGa NPs are coordinated to reducible supports (i.e., TiO_2 and Co_3O_4), forming PtGaPCoCoO@TiO_2 catalysts. PtGaPCoCoO@TiO_2 exhibits high activity and selectivity for hydrogenating nitro compounds to their corresponding amino compounds under mild conditions. The results reveal that the geometrical and electronic effects of P surrounding the PtGaPCo species in PtGaPCoCoO$_x$ are critical for increasing the performance and stability against element poisoning in catalytic reactions. As an electrocatalyst for HER, us-HEA/C achieves an ultrahigh mass activity of 28.3 A mg^{-1} noble metals at −0.05 V (vs. the reversible hydrogen electrode, RHE) in 0.5 M H_2SO_4, which is 40.4 and 74.5 times higher than those of commercial Pt/C and Rh/C catalysts, respectively.

2 | Results and Discussion

2.1 | Controlling PtGa and CoO$_x$ Structures

In this study, we present the synthesis of us-HEA (i.e., PtGaPCoCoO@TiO_2), which incorporates various metal elements under mild conditions via a liquid metal reaction medium. We employed nanoscale sonic dispersion of liquid metals in water (H_2O) as a medium to mix various metal salt precursors (Figure 1A). This was followed by the rapid thermal decomposition and hydrogen reduction of a mixture of metal salt precursors (H_2PtCl_6, $Ga(NO_3)_3$, and Co_3O_4) using ethylene glycol, along with the oxidation of the Ti metal plate. These processes were facilitated by plasma-assisted electrochemical reactions at 0°C for 2 min under irradiation sonication. This procedure was effective for doping transition or noble metals directly onto the TiO_2 support via acoustic cavitation, with a lifetime of less than a microsecond. This was followed by mixing metal elements in liquid metal, resulting in the formation of us-HEA@TiO_2 at 3000 K. The nascent liquid droplets of us-HEA were cooled to room temperature using ice-cold deionized water at the surface–support interfaces to enable rapid quenching (Scheme 1). The resulting alloy catalysts—GaPCoCoO, PtPCoCoO, and PtGaPCoCoO—formed spherical NPs that were firmly anchored onto the porous TiO_x (Figures 1A–D), designed with compact dimensions to facilitate minimal movement of the spillover hydrogen across the TiO_x materials. Furthermore, HR-TEM and HAADF-STEM imaging showed the solid anchoring of PtGaPCoCoO alloy NPs on TiO_x (Figures 1E-H) and demonstrated the presence and distribution of Pt, Ga, Co, and P within individual NPs. According to HAADF-STEM images and energy-dispersive spectroscopy (EDS) elemental mappings of PtGaPCoCoO (ratios of 0.5, 0.5, and 1.0) (Figures 1I-K), the GaPCoCoO, PtPCoCoO, and PtGaPCoCoO

SCHEME 1 | Illustration of the ultrasonic-assisted coincided electro-oxidation–reduction-precipitation process.
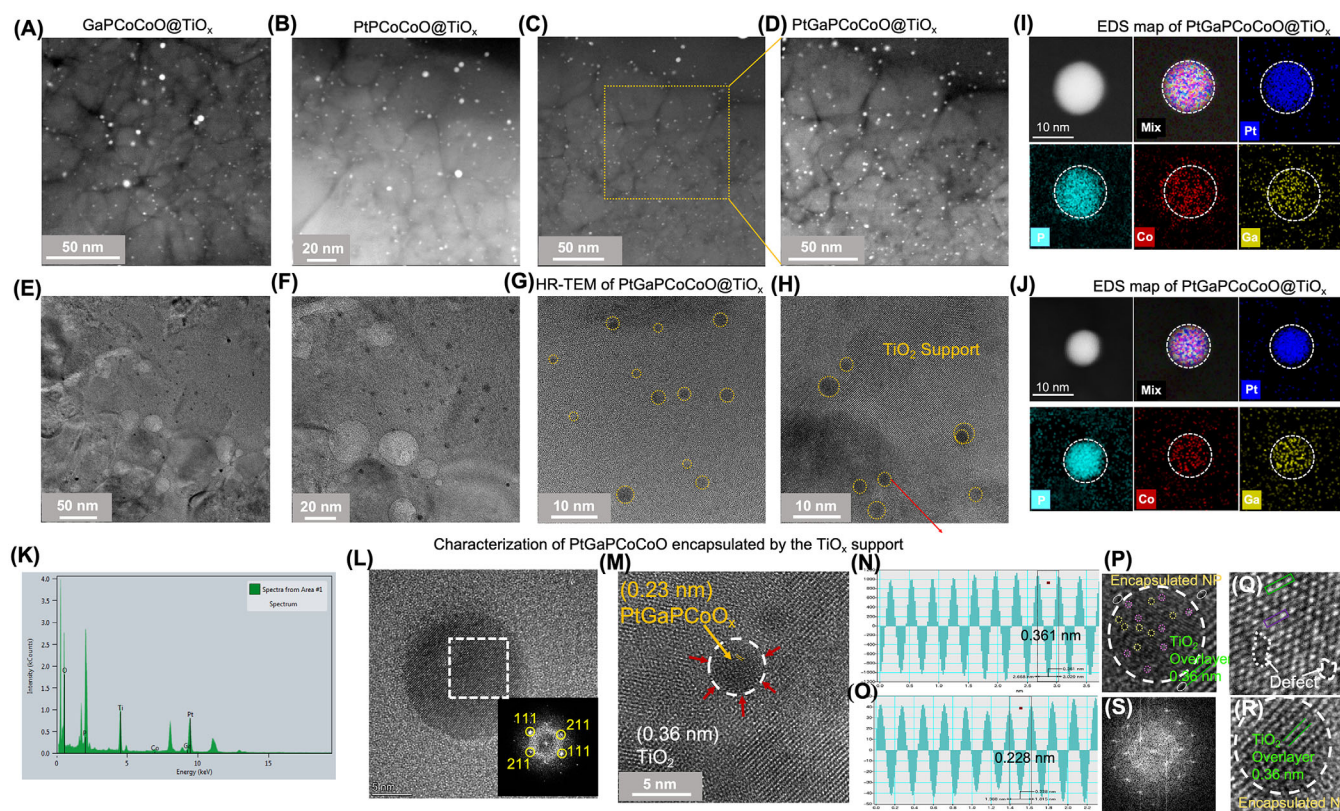

FIGURE 1 | The characterization of PtGaPCoCoO@TiO$_2$ catalysts and coordination of atomically dispersed PtGaPCoCoO to TiO$_x$. HAADF-STEM images of (A) GaPCoCoO, (B) PtPCoCoO, and (C, D) PtGaPCoCoO. (E-H) HR-TEM images of PtGaPCoCoO encapsulated by the TiO$_x$ support. (I, J, and K) HAADF-STEM images of single PtGaPCoCoO NPs and the corresponding EDS maps. (L) and (M) HR-TEM of PtGaPCoCoO, and (N) and (O) d-spacing between adjacent lattice planes. (P-R) HR-TEM images (inset: FFT pattern from the white dotted box area) and EDS of an amorphous NP. The elements are color-coded as follows: blue, Pt; aqua, P; red, Co; yellow, Ga.

NPs were ultrathin and uniformly dispersed on the TiO_x support surface, with mean diameters of approximately 4, 3.3, and 2 nm, respectively, as determined using the ImageJ software (USA).

However, $PtGaPCoCoO@TiO_2$, synthesized without the ultrasonication-plasma effect, exhibited large and agglomerated PtGaPCoCoO NPs, which reduced migration rates (Figure S1.1). The distinct intensities of each atom, observed in well-established atomically dispersed pairs, highlighted the formation of isolated Ga. This was based on element-specific electron scattering cross-sections, where Ga, with a lower Z (atomic number) = 31, exhibited less contrast compared with Pt (Z = 78), which was homogeneously distributed across the TiO_x support (Figure S1.2 and Figures 1L, M). EDS analyses indicated higher concentrations of Ga and Co in the shell, particularly near the side surfaces, than those in the core. EDS data are shown in Figure S1.3. Similar to the initial system, all stoichiometry-tuned systems exhibited uniform mixing of all cations throughout the nanoparticles (Figure S1.4). Additionally, the EDS composition matched qualitatively with the target composition, indicating the stoichiometry of the high-entropy metal NPs. This suggests that PtGaCo components were primarily located near the surface, with Pt more centralized within the core of the NPs, and all metal elements were uniformly distributed within the particles (Figures 1I, J). The loading amount of PtGaPCoCoO on the TiO_x surface was approximately 20 wt.%, as determined by ICP-OES.

The catalyst characteristics of $PtGaPCoCoO@TiO_x$ were further investigated using selected-area electron diffraction patterns (Figure 1L), where the powder X-ray diffraction pattern revealed a single face-centered cubic (fcc) structure with dissimilar peaks at 43.3° 50.4° and 74.1°, corresponding to the (111), (200) and (220) planes, respectively (Figure S2.1–2.3). The three peaks reveal the high crystallinity of the PtGaPCo NPs produced on the surface. A single phase with an fcc structure in XRD, specifically with lattice spacings of 0.23 and 0.36 nm corresponding to the (111) and (211) planes of PtGaPCoCoO-NPs, was identified. Additionally, disordered spherical microdefects on the TiO_x surface, with interplanar crystal spacings of 0.38 nm (Figures M-R), were observed in TEM images (Figure 1M and Figure S1.5 and S1.6). Consequently, $PtGaPCoCoO@TiO_2$, featuring a high PtGaPCo-CoO loading content, uniform distribution, and ultrafine NPs, was effectively synthesized using the ultrasonication plasma method (more information regarding structure in SI and Figures S2.1–S2.3). This synthesis approach surpassed previously reported methodologies for preparing multielement NP materials, such as deposition-precipitation (DP), wet-chemical methods, or Joule heating, in terms of efficiency and effectiveness [11, 12].

Subsequent investigations of the prepared catalysts via XPS corroborated these observations. The Co 2p spectrum, curve-fitted with peaks at 777.44 and 780.01 eV, corresponded to the $2p_{3/2}$ and $2p_{1/2}$ states of metallic Co, respectively (Figure 2A) [12, 13]. Two shakeup satellite peaks at 785.18 and 792.65 eV indicated the presence of Co^{2+} within the PtGaPCoCoO structures. These peaks were attributed to the surface reduction of Co^{3+} and the resultant formation of new oxygen vacancies, whereas the other two peaks at 796.27 and 802.01 eV were associated with Co^{3+} [14, 15]. Moreover, in $PtGa-Co_3O_4$, the binding energies of Co 2p shifted to higher values (~777.90, 781.04, and 786.25 eV), suggesting a change in the electron density around the Co atoms

and the presence of oxygen vacancies in these Co_3O_4 samples. The Pt $4f_{7/2}$ and $4f_{5/2}$ sub-spectra for $Pt-CoO_x$ and $Pt-Ga-CoO_x$, with peak positions at (70.67 eV and 71.95 eV) and (73.55 eV and 75.18 eV), respectively, were identified (Figure 2B). The forward shift in the binding energies for Pt-Ga revealed that alloying Pt with Ga, P, and CoO_x on the TiO_2 surface modified its electronic structure, evidenced by an increase in the vacancy count within the 5d valence band orbital of Pt [16–18]. In the Ga 3d spectra, an asymmetric peak corresponding to metallic Ga^0 was observed at approximately 16.5 eV. The peak for Ga^{3+} states ($\delta < 2$) was observed at approximately 21.77 eV, and the high binding energy of approximately 24.47 eV was attributed to the O2s band (Figure 2c). Shifts of Ga atoms toward high binding energy in $Pt-Ga-CoO_x$ NPs were observed, indicating the reduced electron cloud density of Ga atoms. This could be attributed to the strong electronic mobility of CoO_x, which enhanced electron transfer from electron-donating Ga to Pt sites [18].[18] Additionally, the peaks at 128.98 and 133.4 eV were attributed to metallic state (P^0) and $P-CoO_x$, respectively. The peak at 132.6 eV corresponded to the P^{5+} state (Figure 2D) [19]. To confirm the impact of ultrasonication, the Ti 2p XPS spectrum revealed a shift from 458.18 eV for $PtGaPCoCoO@TiO_x$ synthesized without ultrasonic treatment to 458.28 eV with ultrasonic treatment. This shift indicated the successful formation of metal-rich suboxide layers and Ti^{3+} ions after ultrasonication (Figures 2E-F), signifying the enhanced intensity characteristics of Ti^{3+} species generation [20]. Raman spectroscopy further confirmed these findings (Figure 3A), with the detection of oxygen vacancies in $PCoO@TiO_2$, $GaPCoCoO@TiO_2$, $PtPCoCoO_x@TiO_2$, and $PtGaPCoCoO@TiO_2$ samples. This was evidenced by blue shifts attributable to photon-confinement effects stemming from surface oxygen vacancies. Raman spectra identified four distinct bands at approximately 153.38, 401.43, 522.22, and 646.08 cm^{-1}, corresponding to Raman vibrations in $CoO-TiO_x$ structures [16].

Motivated by these observations, the $Pt-Ga-CoO_x$ system, as a multi-element NP-support configuration, was further evaluated for its wetting properties through water contact angle (CA) measurements. Water droplets on surfaces coated with $PtGaPCoCoO@TiO_x$ under ultrasonic irradiation exhibited enhanced stability over time (Figure 3B). Specifically, the water drop maintained a constant shape with a CA of approximately 52° at room temperature for 25 s. Nyquist plots corroborated these findings, demonstrating the superior durability of $PtGaPCoO@TiO_x$ with ultrasonic irradiation compared to that without ultrasonic irradiation, particularly with increased immersion time in aggressive solutions. This was attributed to the compact structure of TiO_x, comprising both outer and inner layers (Figures 3C, D). In summary, these results unequivocally demonstrate the stability and enhanced surface properties of NPs supported on titanium oxide, achieved through ultrasonication.

2.2 | Hydrogenation of Nitrophenylacetylene

Considering the excellent performance of $PtGaPCoCoO@TiO_x$ in the chemoselective hydrogenation of substituted nitroarenes to yield functionalized anilines, this catalyst may be efficient for the highly selective hydrogenation of nitro groups ($–NO_2$) to amino groups ($–NH_2$), even in the presence of C≡C bonds (Figure 4A). However, the challenge arises when the aromatic
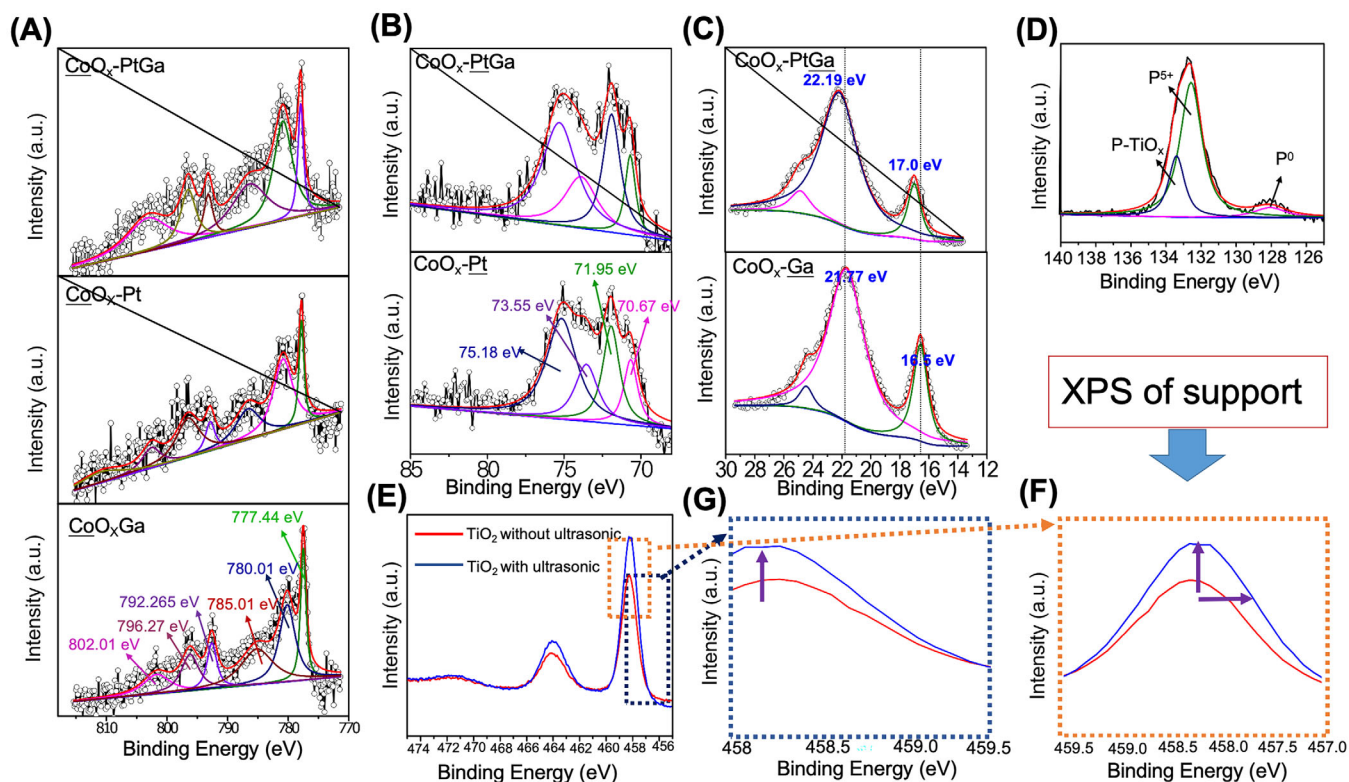
FIGURE 2 | Characterization of elements in different catalysts. XPS patterns of (A) Co 2p, (B) Pt 4f, (C) Ga 3d, and (D) P 2p for GaCoCoO@TiO$_x$, PtCoCoO@TiO$_x$, and PtGaCoCoO@TiO$_x$ catalysts. XPS patterns of (E) TiO$_x$ with and without ultrasonic irradiation, (F) and (G) Enlarged Ti 2p spectrum from (E).
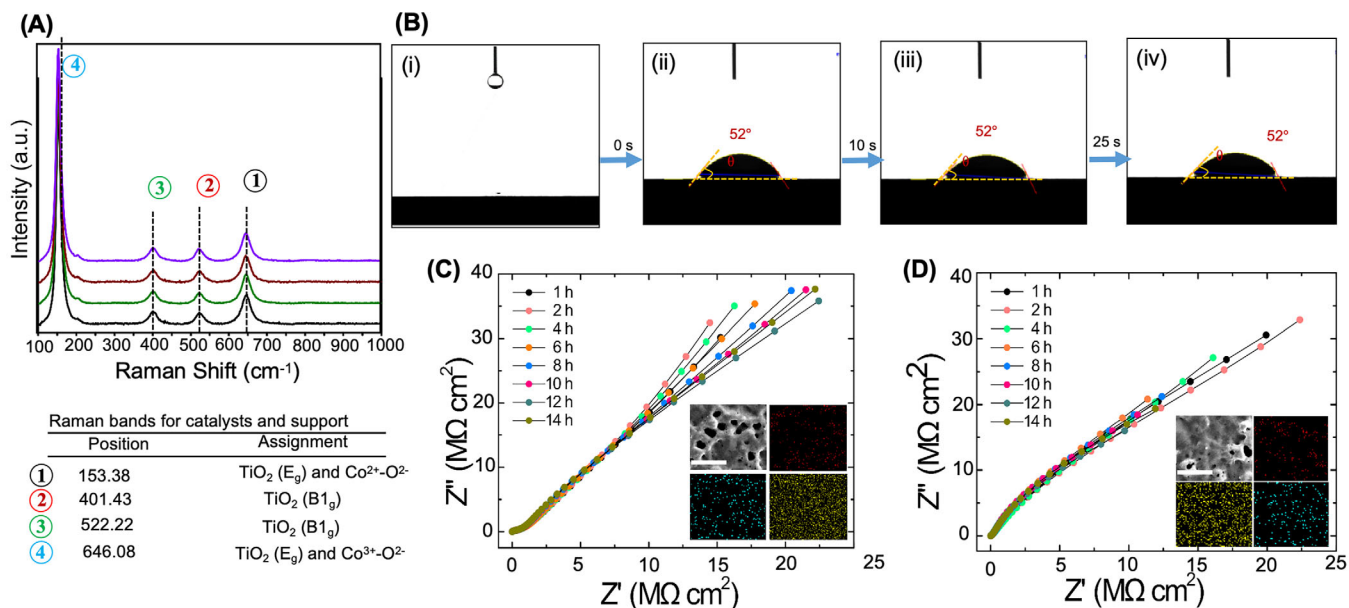
FIGURE 3 | Chemical stability of PtGaPCoCoO@TiO$_x$ catalyst. (A) Raman spectroscopy results and summary of detected bands of prepared GaPCoCoO@TiO$_x$, PtPCoCoO@TiO$_x$, and PtGaPCoCoO@TiO$_x$ catalysts. (B-D) Images of water contact angles of TiO$_x$ treated with and without ultrasonic irradiation (control sample with the ultrasonic-based surface) and impedance responses of TiO$_x$ in the corrosive solution presented in the Nyquist plot.
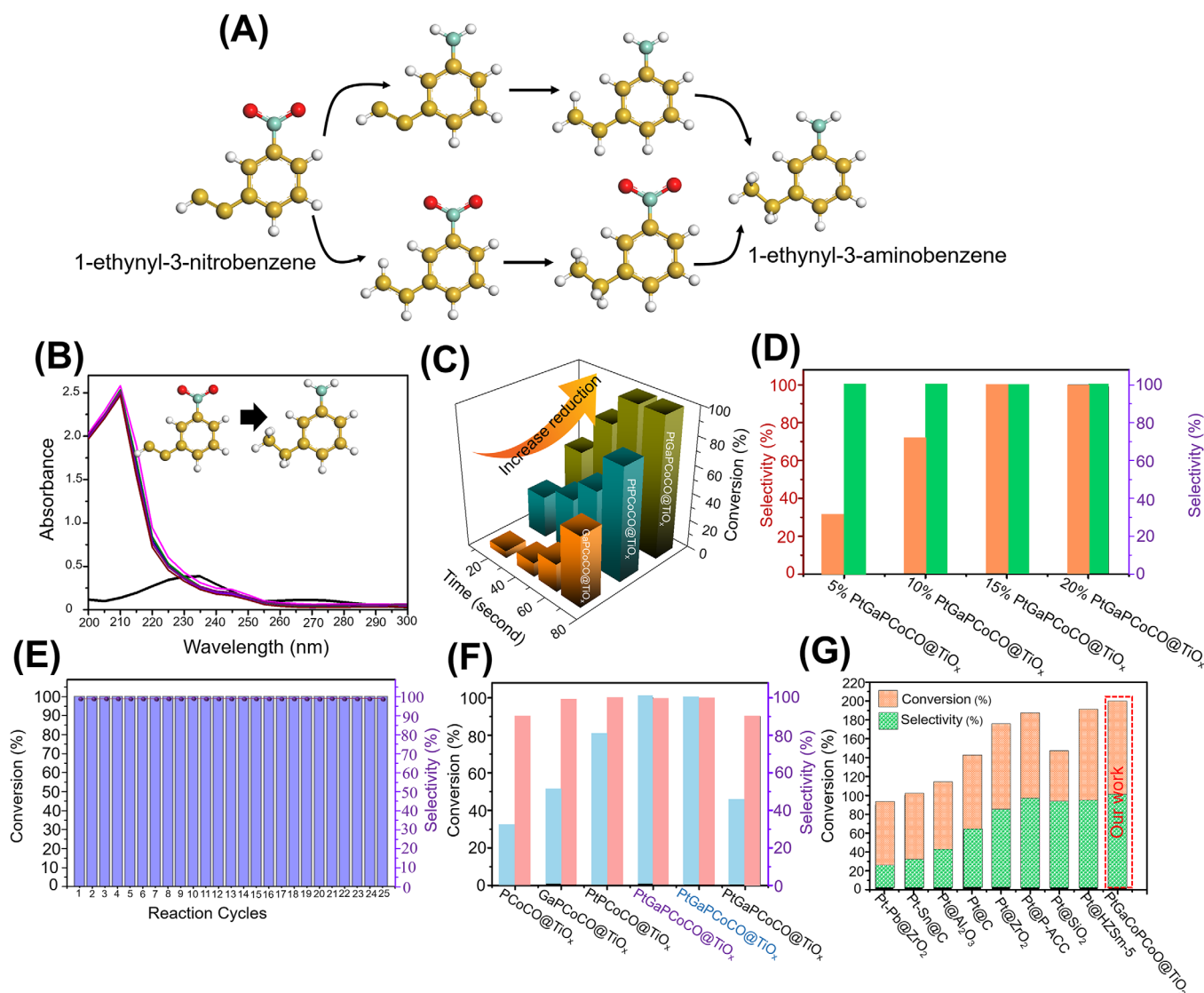
FIGURE 4 | Catalytic performance of PtGaPCoCoO@TiO$_x$ catalysts. (A, B) Reaction reduction and UV–vis absorption spectra of 1-ethynyl-3-nitrobenzene. (C) Catalytic performance of GaPCoCoO@TiO$_x$, PtPCoCoO@TiO$_x$, and PtGaPCoCoO@TiO$_x$ for the hydrogenation of 1-ethynyl-3-nitrobenzene. (D) Comparison of the catalytic activities at various Pt loadings in the catalysts (i.e., 5%PtGaPCoCoO@TiO$_x$, 10%PtGaPCoCoO@TiO$_x$, 15%PtGaPCoCoO@TiO$_x$, and 20%PtGaPCoCoO@TiO$_x$). (DE) Reusability profiles of PtGaPCoCoO@TiO$_2$ for the hydrogenation of 1-ethynyl-3-nitrobenzene to 1-ethynyl-3-aminobenzene. (F) Catalytic activities of different catalysts for 1-ethynyl-3-nitrobenzene to 1-ethynyl-3-aminobenzene at various reaction conditions. (G) Comparison of the catalytic performance of PtGaPCoCoO@TiO$_2$ with that of recently reported Pt-based catalysts

ring contains various reducible groups such as ketones, nitriles, amides, aldehydes, halogen atoms, olefins, and, most notably, highly sensitive alkynes. Reducing the nitro group while preserving these other reducible functional groups poses a significant challenge [21]. First, the selective hydrogenation of 1-ethynyl-3-nitrobenzene (1-Et-3-NB) to 1-ethynyl-3-aminobenzene (1-Et-3-AB) was examined under optimized catalytic conditions. The catalytic transformation of 1-Et-3-AB and the reaction progress were monitored using UV–vis spectroscopy, which indicated a decrease in the intensity of bands at 269 and 232 nm for 1-Et-3-NB and the emergence of peaks at 209 and 245 nm (Figures 4B, C) corresponding to the formation of 1-Et-3-AB. The hydrogenation of 1-ethynyl-3-nitrobenzene (5 mmol) was performed using –4 mg of the catalyst and two equivalents of NaBH$_4$ in methanol (10 mL) as the solvent at room temperature, following the optimized reduction reaction conditions. The PtGaPCoCoO@TiO$_x$ catalyst

demonstrated exceptional efficiency, achieving 99% conversion and 99% selectivity toward 1-Et-3-AB within 60 s (Figure 4D). This suggested an enhancement in the electron density of PtGa in the presence of Co and P, leading to the hypothesis that the bifunctional effect could affect the electronic state of the multi-element NPs and the selectivity toward 1-Et-3-AB. It was inferred that activating H$_2$ molecules on PtGaPCoCoO required significantly lower dissociation energy than that for PtPCoCoO or GaPCoCoO, where CoO consumed more hydrogen species [22].

XPS analysis revealed that the Pt NPs were electron-deficient, with the Pt 4f$_{7/2}$ peaks in the PtGaPCoCoO$_x$ catalyst shifting to higher energies, compared with those of metallic PtGaP-CoCoO. With GaPCoCoO@TiO$_2$ and PtPCoCoO@TiO$_2$, both conversion and selectivity for 1-Et-3-NB to 1-Et-3-AB (Figure 4D and Figure 2A) were notably lower. The hydrogenation outcomes

indicated that PtGaPCoCoO, with its negatively charged Pt NPs, tended to selectively reduce the NO_2 group to valuable 1-Et-3-AB (Figure 4D). The selectivity for this reduction was further enhanced in the PtPCoCoO@TiO$_x$ catalyst, attributed to the CoO promoter-induced increase in O_v sites via the hydrogen spillover effect [23, 24].

Next, the catalytic activities of PCoCoO$_x$@TiOx and TiO$_x$ were compared to determine the presence of active catalytic sites. The results revealed negligible product formation (~0.8%) (Table S1.1), indicating that the catalytic activity primarily originated from PtGaPCo NPs. When the PtGaPCoCoO$_x$@TiO$_x$ catalyst, prepared via conventional methods such as DP or incipient wetness impregnation, was subjected to the same experimental conditions, a significantly lower selectivity of 70.5% was achieved for 1-ethynyl l-3-aminobenzene. This outcome suggested that the microenvironment of the TiO$_x$ surface defects and the diminutive size of the PtGaPCo NPs were advantageous for achieving high conversion and selectivity in the hydrogenation of nitroarenes. PtGaCoCoO$_x$@TiO$_x$, containing lower Pt amounts (theoretical load capacity: 15%), was evaluated for its ability to produce 1-ethynyl l-3-aminobenzene. The catalyst with a higher Pt loading exhibited a more rapid conversion rate, achieving higher conversion within 1 min. This observation underscored the superior catalytic performance of active catalysts with high Pt NP loadings (Figure 4D), further emphasizing the critical role of Pt content in catalyzing the selective hydrogenation process.
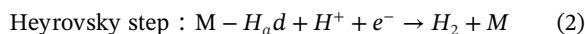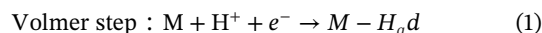
The reusability of the PtGaPCoCoO@TiO$_x$ catalyst was investigated through the reductive formylation of 1-ethynyl-3-nitrobenzene as a probe reaction. To prepare the catalyst for subsequent runs, it was washed with ethanol twice and dried in an oven at 50°C. The reduction reactions proceeded under optimized conditions. Remarkably, the PtGaPCoCoO$_x$@TiO$_x$ catalyst maintained its activity without significant degradation even after 25 consecutive cycles in the production of 1-ethynyl-3-nitrobenzene, showcasing its high stability and intrinsic reusability (Figure 4F). To verify the stability of the catalyst, STEM characterizations of the spent PtGaPCoCoO@TiO$_x$ catalyst after 25 cycles were conducted (Figures S1.7 and S1.8). The STEM images revealed no agglomeration, suggesting that the strong metal-support interactions and the morphology of the catalyst remained largely unchanged compared with the fresh catalyst. This observation confirmed its exceptional durability. Additionally, the results indicated that the environment around the PtGa active sites could be modified through encapsulation with a CoO$_x$ shell. Further studies on PtGaPCoCoO@TiO$_x$ under various conditions, including UV and ultrasonic irradiation during catalytic reactions, demonstrated increased conversion rates compared with other conditions (Figure 4F, G). A comparison of the conversion rates using different catalysts, as reported in the literature, revealed that PtGaPCoCoO@TiO$_x$ exhibited superior catalytic efficiency among Pt-based catalysts (Table S1.2) [25–30].

To understand the reactivity of the PtGaPCoCoO@TiO$_x$ surface and the role of atomic sites, simulations were conducted to investigate the adsorption of 1-Et-3-NB on ~2 nm NPs. The NP model was built based on the geometry-optimized periodic model. 1-Et-3-NB (Figure 4) was preferentially adsorbed at heteroatom sites (0.0-0.15 ps) in PtGaPCoCoO@TiO$_x$, particular at Ga and

Pt atoms. MD calculations show that 1-Et-3-NB has a strong affinity for Pt/Ga/P-rich sites. This probe reaction highlights the competitive nature of the vinyl group (C≡C) in forming NH_2 groups, with the reaction pathway shown in Figures 5A, B.

2.3 | Hydrogen Evolution Reaction (HER) Performance of the Electrocatalysts

The HER performances of all the materials were measured using a standard three-electrode system. PtGaPCoCoO@TiO$_x$ performed the best as an HER material in 0.5 M H_2SO_4 aqueous solution (Figure 6A), with an overpotential of 187 mV at a current density of 10 mA cm^{-2}. This was due to the synergistic effect of Ga and Pt and their interactions with Co_3O_4. PtPCoCoO@TiO$_x$ (η_{10} = 354 mV), GaPCoCoO@TiO$_x$ (η_{10} = 480 mV), and CoO@TiO$_x$ (η_{10} = 640 mV) had the lowest HER activities compared with the Ga/Pt/Co_3O_4 material. In addition, Tafel plots for PtGaPCoCoO@TiO$_x$ showed a slope value of 152 mV dec^{-1} (Figure 6B). The Tafel slope suggests that the reaction mechanism of the material is based on the following two steps described by Volmer and Heyrovsky [31]:

$$\text{Volmer step}：M + H^+ + e^- \rightarrow M - H_a d \qquad (1)$$

$$\text{Heyrovsky step}：M - H_a d + H^+ + e^- \rightarrow H_2 + M \qquad (2)$$

Here, M denotes the number of active sites in the catalyst. First, the H^+ ion attaches to the active site of the catalyst (H_{ad}). Similarly, another H^+ ion attaches to the active site to produce an H_2 molecule. Therefore, adsorption on the active sites is the rate-determining step in this type of reaction. The Tafel slopes gradually increased for the other catalysts, indicating sluggish reaction kinetics. The values were 182, 186, and 187 mV s^{-1} for PtPCoCoO@TiO$_x$, GaPCoCoO@TiO$_x$, and CoO@TiO$_x$, respectively.

To gain insights into the nature of the catalytic active sites, the double-layer capacitance values of all electrocatalysts were measured. From the results presented in Figure 6C, double-layer capacitance is directly proportional to the electrochemically active surface area, which quantitatively measures the number of active sites available for catalysis. Moreover, the electrochemical surface area (ECSA) is a critical parameter for evaluating the active site density, as it directly reflects the population of electroactive sites engaged in the reaction, as shown in Figure 6D [32]. This assessment was conducted using cyclic voltammetry (CV) measurements within the voltage range of 0.05–0.15 V (vs. RHE) at varying scan rates (as detailed in Figure S1.9S). By plotting the change in current density (ΔJ), calculated as the difference between the anodic current density (Ja) and cathodic current density (Jc), ledJ_c), against the scan rate, it was possible to derive the double-layer capacitance (Cdl) [33]. The C_{dl} values are 0.25, 0.19, 0.16, and 0.15 mF cm^{-2} for PtGaPCoCoO@TiO$_x$, PtPCoCoO@TiO$_x$, GaPCoCoO@TiO$_x$, and PCoO@TiO$_x$, respectively. The ECSAs are 3.75, 4, 4.75, and 6.25 cm^2 for PCoO@TiO$_x$, PtPCoCoO@TiO$_x$, GaPCoCoO@TiO$_x$, and PtGaPCoCoO@TiO$_x$
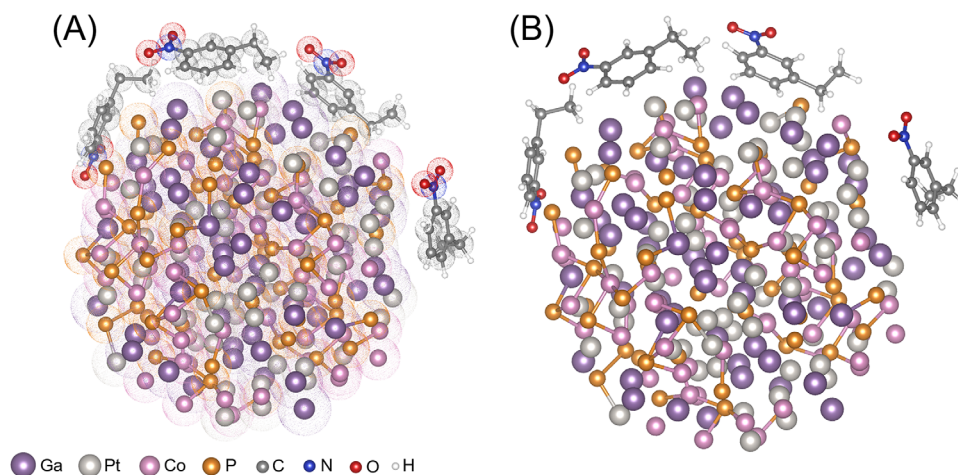
FIGURE 5 | DFT calculations. (A and B) Atomistic model for the adsorption of four 4-NP molecules on the surface of a PtGaCoP nanoparticle. Face-on molecular adsorption and some degree of local surface rearrangement contribute to minimize the adsorption energy. Van der Waals radii are shown in (A).
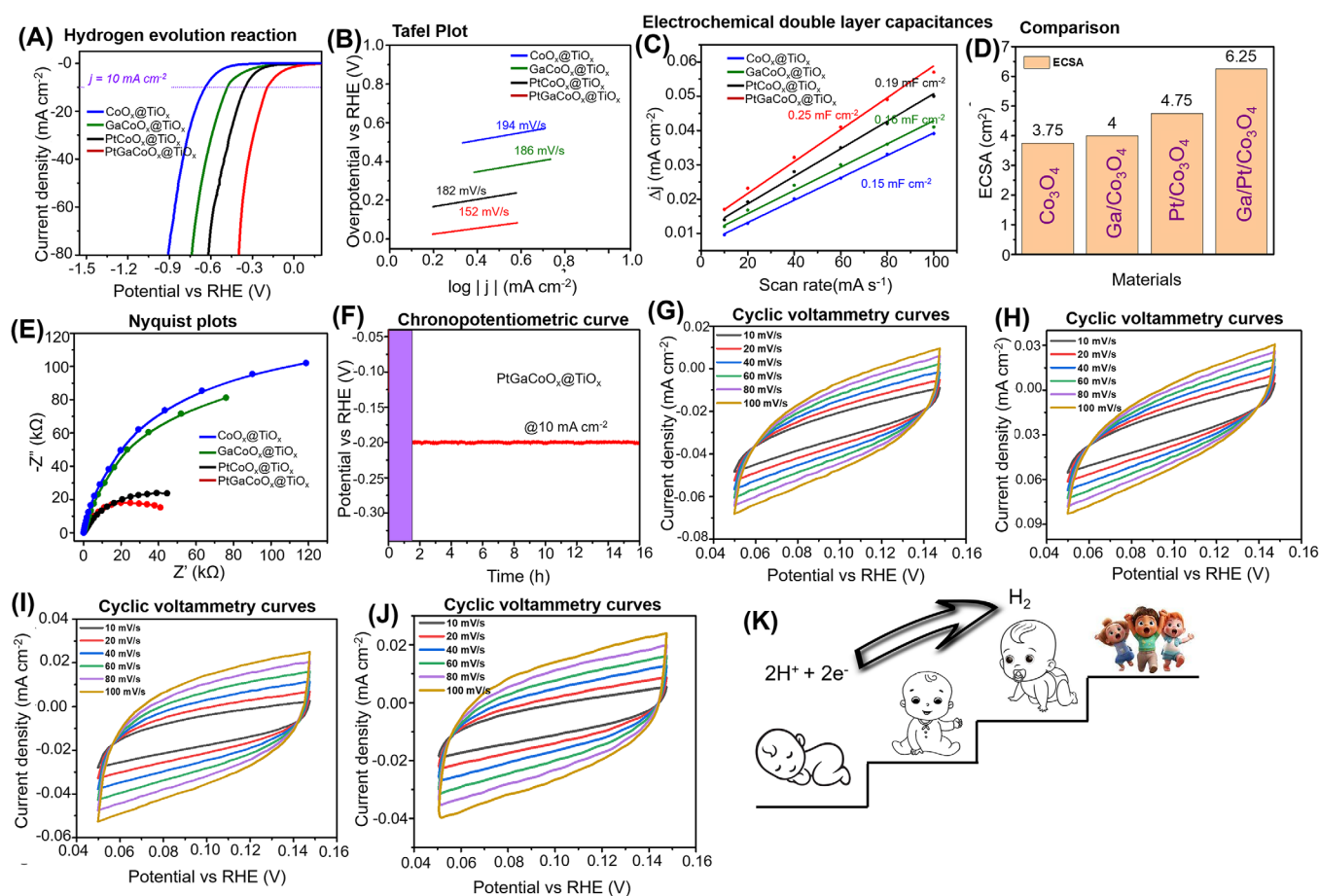

FIGURE 6 | Electrochemical property of PtGaPCoCoO@TiO$_x$. HER experimental results for the electrocatalysts in 0.5 M H$_2$SO$_4$. (A) Linear sweep voltammetry curves, (B) Tafel plots, (C) double-layer capacitance (C_{dl}) values, (D) electrochemical surface areas, (E) Nyquist plots, and (F) chronopotentiometric stability analysis CV curves in the double layer regions for the prepared catalysts. Cyclic voltammograms of (G) CoO@TiO$_x$, (H) PtPCoCoO@TiO$_x$, (I) GaPCoCoO@TiO$_x$, and (J) PtGaPCoCoO@TiO$_x$. (K) Catalytic activity in the presence of multielement nanoparticles.

respectively, calculated as follows [34]:

$$\text{ESCA} = \frac{C_{dl}}{C_s} = \frac{C_{dl}}{0.04 \, \frac{mF}{cm^2} \text{ per cm}^2} \quad (3)$$

where C_{dl} is the double-layer capacitance, and C_s refers to the specific capacitance. For a flat surface, C_s is typically considered to be 0.04 mF cm^{-2} [35]. The double-layer CV curves shown in Figure S1.9 underscore the presence of a high number of catalytically active sites in PtGaPCoCoO@TiO$_x$. This characteristic enables the catalyst to facilitate more rapid H$^+$ diffusion to the active sites for the catalytic reaction, outperforming other synthesized materials efficiently.

Electrochemical impedance spectroscopy was conducted on all samples to further investigate their electrochemical behavior, with the findings presented in Nyquist plots (Figure 6E). The PtGaPCoCoO@TiO$_x$ composite exhibited a notably lower charge transfer resistance (R_{CT}) than those of other samples, underscoring its superior charge transfer capabilities during the electrocatalytic HER. Figure 6F-J shows a chrono-potentiometric stability analysis for the PtGaPCoCoO@TiO$_x$ sample at −10 mA cm^{-2}. It shows excellent stability even after 16 h, where the first 1.5 h is the time required for the activation phase to reach a fixed potential (Figure 6G-K). This level of stability, coupled with the low charge transfer resistance, positions PtGaPCoCoO@TiO$_x$ as a highly effective catalyst for the HER, showcasing its potential for practical applications in electrocatalysis.

U-SEO-P is a physicochemical process that occurs at the anode–electrolyte interface (i.e., Ti alloy) and typically produces a robust coating on the substrate surface owing to electrochemical reactions, plasma chemical reactions, and thermal diffusion in the electrolyte and at the substrate–electrolyte interface. Notably, PtGaPCoCoO and the TiO$_x$ support are formed concurrently in situ on the Ti plate. This occurs via high local temperature decomposition and reduction of precursors, with ethane-1,2-diol acting as the reducing agent, as well as oxidation of the Ti substrate owing to the high-voltage discharge. Combining ultrasonic irradiation, such as cavitation, increases local temperature and pressure differentials. In addition, chemical reactions are enhanced by the hydroxyl radicals and hydrogen produced, as summarized in the following equation.

$$H_2O + \text{ultrasound} \rightarrow e^-_{aq}, H_3O^+, H^{\cdot}, H_2, OH^{\cdot}, H_2O_2 \quad (4)$$
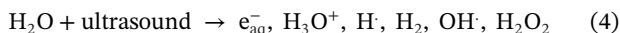
The volume and lifetime of the bubbles are determined by the ultrasonic power intensity in aqueous media. Therefore, plasma sparks produced under ultrasonic irradiation and electrochemical methods were smaller and had a shorter lifetime than those obtained without ultrasonic irradiation. Metal atoms reduced from metal salts and metal oxides could not spread over large distances, which facilitated the aggregation of PtGaPCoCoO NPs on the TiO$_x$ surface owing to the very short-lived localized plasma discharges. Hence, cavitation enhanced the local reduction reactions and agitation through heat transfer from gas bubbles, accelerating the formation and nucleation processes on the TiO$_x$ surface and increasing the concentration of seeds (Figure S1.10). This strategy resulted in the homogeneous mixing of dissimilar metal elements throughout the NPs without obvious phase separation or elemental segregation. This indicates the suc-

cessful preparation of a single us-MEA-NP on the support surface (more details about its structure are mentioned in Supporting Information).

U-SEO-P was employed to elucidate the synthesis and miscibility of the three elements (Pt, Ga, and Co) in the PtGaPCoCoO@TiO$_x$ catalyst. This method facilitated the formation of a uniform us-HEA by generating high local discharge temperatures through ultrasonic irradiation. Such conditions significantly enhanced the entropy contribution (TΔS_{mix}) while reducing the enthalpy (ΔH_{mix}) (Figures 7A, B) [36]. This thermodynamic balance promoted the stabilization of solid solutions.

Figure 7B displays the map of ΔS_{mix} for the PtGaCo alloy, highlighting that the ΔS_{mix} value for alloy compositions is closer to the central region peaks at the center. This phenomenon suggests that the energy gain, derived from the high local temperature and ultrasonic irradiation, is substantial for ΔG_{mix} and ΔS_{mix} to stabilize a multi-component alloy with equimolar fractions of its constituents. This stabilization follows Richard's rule [37], indicating that mixing multiple elements in equal proportions can form a stable HEA.

The equation for ΔS_{mix} in the context of us-HEA, assuming a condition of high entropy, is applied only at high temperatures [38].

$$\Delta S_{mix} = R \ln n \quad (5)$$

As ΔS_{mix} scales with ln n (e.g., n is the total number of the constituent elements), a larger ΔS_{mix} can be achieved for NP alloys with a greater number of metal elements, thus augmenting the opportunity of forming solid solutions, according to Equation 1. We anticipated using the effect of local discharge temperature to design the us-HEA under different temperature reductions (1000–4000°C). ΔG_{mix} in the range temperature (i.e., 1000–4000°C) improves the formation of us-HEA, coming up to three immiscible elements (Pt, Ga, and Co) via the synergy of ultrasonic irradiation and high discharge temperature (Figure 7C–H). However, a significant increase in temperature triggered the rapid thermal decomposition and reduction of the metal salt precursors to metals, leading to the completion of the formation of us-HEA upon fast quenching in less than 60 s. Mixing Gibbs free energy (ΔG_{mix}) is the addition of the contributions of mixing enthalpy (ΔH_{mix}) and mixing entropy (ΔS_{mix}),

$$\Delta G_{mix} = \Delta H_{mix} - T\Delta S_{mix} \quad (6)$$

ΔH_{mix} is mainly related to atomic bonding energy from a quasi-chemical model and does not depend on the number of components (n) in the system, as shown in Figure 7I. Introducing more components into a system effectively increases ΔS_{mix} due to the higher configurational entropy [38]. When plotting ΔG_{mix} against temperature [39], ΔS_{mix} corresponds to the slope of the curve. Consequently, the reduction of ΔG_{mix}, or in other words, the stabilization of a single phase by increasing temperature, is most pronounced for systems with $n = 3$. The influence of ΔH_{mix} on ΔG_{mix} is significant at lower temperatures, around 1000 K, but diminishes at temperatures exceeding 2000 K [40, 41]. As a result, at high temperatures induced by plasma discharge and ultrasonic irradiation, ΔG_{mix} can be effectively altered by ΔS_{mix}.
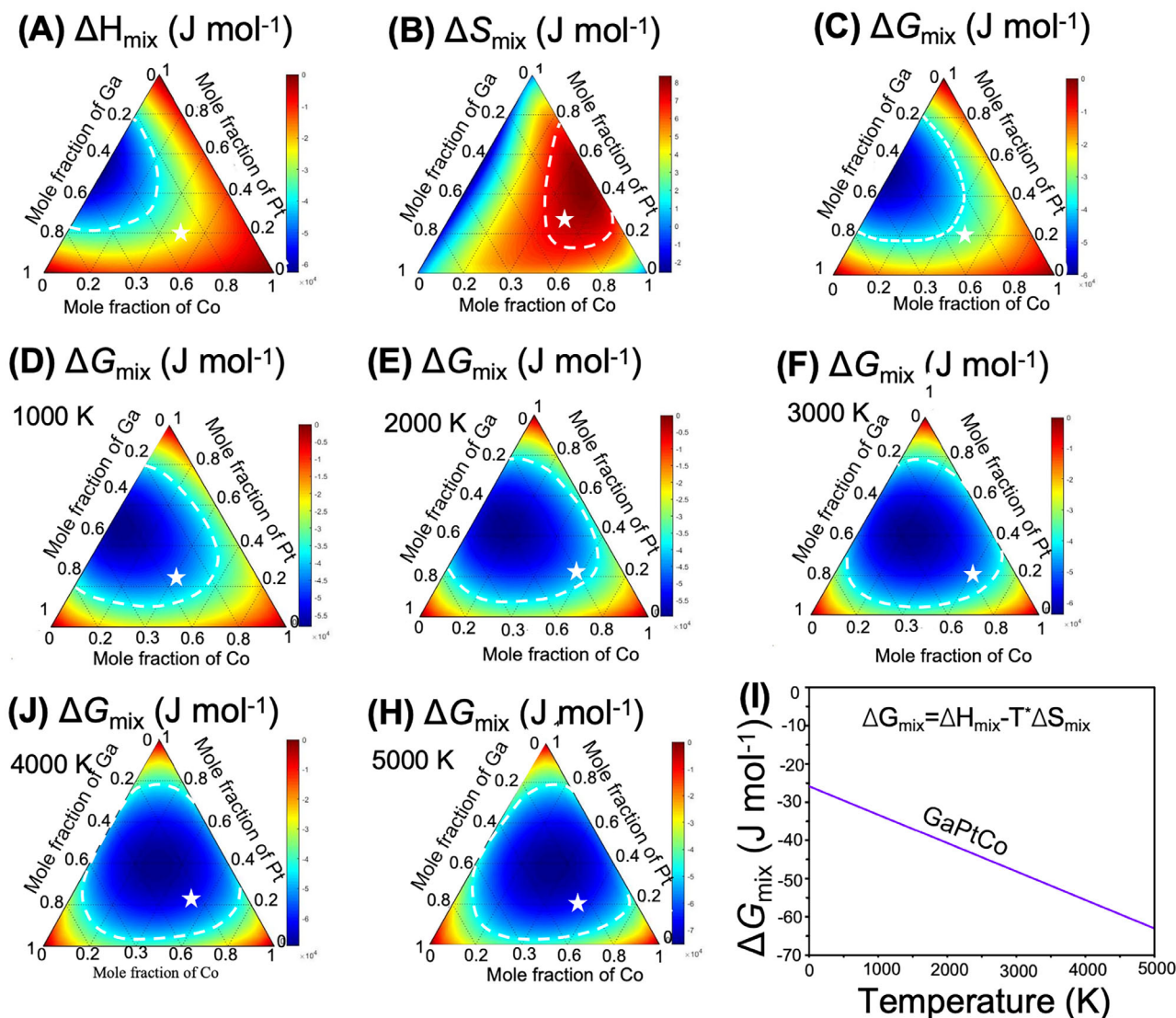
FIGURE 7 | Computational alloy formation prediction of us-HEA. (A) Contour plot of mixing enthalpy (ΔH_{mix}) (j/mol K) of a PtGaCo system. (B) Contour plot of mixing entropy (ΔS_{mix}) (j/mol K) of a PtGaCo system. (C-H) Temperature-dependent Gibbs free energy (ΔG_{mix}) of PtGaCo system-NPs derived from thermodynamic calculations. (I) Temperature-dependent Gibbs free energy (ΔG_{mix}) of PtGaCo derived from thermodynamic calculations.

These conditions facilitate severe in-depth diffusion and lattice distortion, stabilizing the structure of us-HEA against elemental aggregation and nanoscale phase separation, confirming the formation of a solid-solution structure.

The higher rate of ΔG_{mix} reduction in systems with a higher n ensures that the lattice strain can be readily overcome at very high temperatures ($\sim$2000 K), facilitated by both plasma discharge and ultrasonic irradiation. Beyond merely increasing the temperature, the vibrational energy provided by ultrasonic waves and plasma discharge disrupts the system, allowing the contribution of ΔS_{mix} to surpass that of ΔH_{mix}. This forms a completely miscible and uniform us-HEA NP on the TiO$_x$ surface (Figure 7I).

This strategy paves the way for preparing nanomaterials and alloys with customizable compositions, catering to a broad spectrum of applications. Achieving an optimized temperature range between 1500 and 4000 K is crucial for synthesizing uniform us-

HEAs on TiO$_x$, providing the necessary energy to mix all metallic elements into a single NP and preventing agglomeration.

The approach also extends to immobilizing us-HEAs on various metal oxides, including NiO, Al$_2$O$_3$, In$_2$O$_3$, and MgO, demonstrating the versatility of this method across different numbers of metals and metal oxide supports without phase separation. This highlights the potential of the U-SEO-P technique in fabricating and immobilizing us-HEAs on diverse supports, underscoring its applicability in creating homogeneous alloys for a wide range of uses [42, 43].

3 | Conclusions

We successfully developed a universal template-assisted U-SEO-P to produce thoroughly contacted PtGaPCoCoO@TiO$_x$ catalysts. This approach allowed for precisely adjusting CoO$_x$–PtGa proximity by altering the deposition sequence and wall

thickness of the porous TiO_x surface. We discovered that adding PtGaPCoCoO enhanced the hydrogen spillover effect, leading to an increase in O_v. These vacancies served as active adsorption sites for nitro compounds through $N = O$ bonds, thereby significantly enhancing the selectivity toward 1-Et-3-NB in the hydrogenation reactions to 1-Et-3-AB. Interestingly, this hydrogen spillover effect remained effective even after additional oxide layers were selectively deposited on the PtGaPCoCoO promoter using U-SEO-P to cover its surface completely. Our findings demonstrated a potent method utilizing U-SEO-P to design dual-component catalysts that exhibited specific promoter-metal closeness and assembled metal and oxide supports. This methodology is instrumental in uncovering the fundamentals of dual-component synergy, elucidating the enhancement mechanism, and identifying the true active sites within the catalyst structure.

4 | Experimental Section

4.1 | Preparation of Catalysts

The PtGaPCoCoO@TiO$_2$ catalyst was prepared by one-pot ultrasonic-assisted coincided electro-oxidation-reduction-precipitation using bulk by applying a frequency of 60 Hz, an AC power supply of 20 kW, and ultrasonic irradiation at 28, 40, and 138 kHz at 0°C using a water cooling system during the U-SEO-P process to maintain the electrochemical reactions for 120 s to a Ti anode (bulk Ti) (purity: 99.8%, 20×15×3 mm^3) immersed in a phosphate-based electrolyte (3 gL^{-1} ethylenediaminetetraacetic acid, 7 gL^{-1} K$_3$PO$_4$, 5 gL^{-1} KOH, 10 gL^{-1} K$_3$PO$_4$, and 35 gL^{-1} C$_2$H$_6$O$_2$ in 2 L of deionized water (pH = 11.5). U-SEO-P is a conventional method used to prepare a reducible TiO$_2$ support on the Ti substrate in the existence of H$_2$PtCl$_6$·6H$_2$O (99.5%; Merck), Ga(NO$_3$)$_3$·9H$_2$O (98.5%; Merck), and Co$_3$O$_4$ (99.5%; Merck) as precursors. The loading of Pt, Ga, and Co$_3$O$_4$ NPs was controlled at 0.25 weight % (molar ratio of PtGaPCoCoO@TiO$_2$, 1:3). For the preparation of PtGaPCoCoO@TiO$_2$ catalysts, H$_2$PtCl$_6$·6H$_2$O, Ga(NO$_3$)$_3$·9H$_2$O, and Co$_3$O$_4$ (18 nm) were dissolved in deionized water and ethyl alcohol solution. Utilizing a stirrer alongside ultrasonic irradiation, fine bubbles were generated within the solution to ensure a uniform dispersion of NPs. Subsequently, the catalysts were washed in 10 mL of ethanol for various durations and dried at 60°C overnight. In the U-SEO-P process, the plasma sparks exhibited smaller sizes and extended lifetimes compared with those generated in the SEO-P method, which lacks ultrasonic irradiation. This effect was crucial in preventing the wide dispersal of metallic atoms post-reduction by ethylene glycol, thereby inhibiting the aggregation of PtGaPCoCoO-NPs on the surface of reducible TiO$_2$ supports because of the minimal size and brief lifespan of localized plasma discharges. The metal content within the catalysts was determined by ICP-AES (PerkinElmer, Optima 8300). TEM images were recorded using a Tecnai F20 microscope (FEI, Japan). The physicochemical characteristics of the catalysts were assessed by field-emission scanning electron microscopy (Hitachi, S-4800), X-ray diffraction (XRD; D-MAX 2500, Rigaku, Japan), X-ray photoelectron spectroscopy (XPS; ESCA 2000, VG Microtech, UK), focused ion beam electron microscopy (Helios Nanolab 600, Country), g Fourier-transform infrared (Bio-Rad, Excalibur Series FTS 3000) spectroscopy, Raman spectroscopy (Horiba, XploRA Plus,

Country), and liquid chromatography–mass spectroscopy (Q Exactive Vanquish, Thermo Fisher, USA).

4.2 | Reactivity Test of PtGaCo$_3$O$_4$@TiO$_2$

The catalytic selectivity and recyclability of PtGaPCoCoO@TiO$_2$ in the hydrogenation of nitro compounds were evaluated by mixing 80 mL of an aqueous 1-ethynyl-3-nitrobenzene solution (1.35 mM) with approximately 5.0 mg of PtGaPCoCoO@TiO$_2$ under vigorous stirring at 25°C. At predetermined intervals, approximately 3 mL of the reaction mixture was sampled, immediately analyzed using a UV–vis spectrophotometer (Cary 5000, Agilent) to monitor absorbance changes at 400 nm, and reintroduced into the solution. Furthermore, a recyclability test was performed post-reaction by extracting the catalyst and cleaning it with water and ethanol to evaluate its reusability.

4.3 | Computational Method

In this calculation, we used the ATAT code to create a special quasirandom structure (SQS) of the PtGaCoP alloy (HEA) from a 3 × 2 × 1 supercell of the Pt (111) surface. The ATAT code uses a Monte Carlo strategy to find the best match for the pair correlation functions of the alloy of interest. Correlation functions capture the atom arrangements in the alloys and are therefore suitable fingerprints for searching crystal models. The Monte Carlo strategy enabled us to obtain the first model for the adsorption of four 4-NP molecules on a rigid 1-nm PtGaCoP spherical NP. A combination of Dreiding and UFF force fields were used. Molecular translations and rotation were assigned equal probability, for a total of one million moves. The resulting geometry was subsequently optimized. Interatomic force calculations were based on the transferable tight-binding GFN xTB, as implemented in cp2k [41–47].

4.4 | Electrochemical Measurements

More details are provided in the Supporting Information.

4.5 | Thermodynamic Calculations

More details are provided in the Ref 45.

Conflicts of Interest

The authors declare no conflicts of interest.

References

1. J. Zhang, Z. Gao, S. Wang, et al., "Origin of Synergistic Effects in Bicomponent Cobalt Oxide-Platinum Catalysts for Selective Hydrogenation Reaction," *Nature Communications* 10, no. 1 (2019): 4166.

2. W. Al Zoubi, Y. Sheng, I. Hussain, et al., "Synthesis and machine learning prediction of high entropy multi-pronciple element nanoparticles," *Small* 21, no. 22 (2025): 2501444.

3. N. M. Briggs, L. Barrett, E. C. Wegener, et al., "Identification of Active Sites on Supported Metal Catalysts With Carbon Nanotube Hydrogen Highways," *Nature Communications* 9, no. 1 (2018): 3827.

4. T. N. Phaahlamohlaka, D. O. Kumi, M. W. Dlamini, et al., "Effects of Co and Ru Intimacy in Fischer-Tropsch Catalysts Using Hollow Carbon Sphere Supports: Assessment of the Hydrogen Spillover Processes," *ACS Catalysis* 7, no. 3 (2017): 1568–1578.

5. W. Karim, C. Spreafico, A. Kleibert, et al., "Catalyst Support Effects on Hydrogen Spillover," *Nature* 541, no. 7635 (2017): 68–71.

6. Z. Li, M. Zhang, X. Dong, et al., "Strong Electronic Interaction of Indium Oxide With Palladium Single Atoms Induced by Quenching Toward Enhanced Hydrogenation of Nitrobenzene," *Applied Catalysis B: Environmental* 313 (2022): 121462.

7. Z. Wu, B. C. Bukowski, Z. Li, et al., "Changes in Catalytic and Adsorptive Properties of 2 Nm Pt3Mn Nanoparticles by Subsurface Atoms," *Journal of the American Chemical Society* 140, no. 44 (2018): 14870–14877.

8. W. Cai, R. Mu, S. Zha, et al., "Subsurface Catalysis-Mediated Selectivity of Dehydrogenation Reaction," *Science Advances* 4, no. 8 (2018): 541.

9. Y. Wang, H. Li, S. Di, et al., "Constructing Long-Cycling Crystalline C_3N_4-Based Carbonaceous Anodes for Sodium-Ion Battery via Nconfiguration Control," *Carbon Energy* 6, no. 1 (2023): 388.

10. W. Al Zoubi, A. W. Allaf, B. Assfour, and Y. G. Ko, "Concurrent Oxidation-Reduction Reactions in a Single System Using a Low-Plasma Phenomenon: Excellent Catalytic Performance and Stability in the Hydrogenation Reaction," *ACS Appl Mater Interfaces* 14, no. 5 (2022): 6740–6753.

11. K. Kusada, M. Mukoyoshi, D. Wu, and H. Kitagawa, "Chemical Synthesis, Characterization, and Properties of Multielement Nanoparticles," *Angewandte Chemie International Edition* 61, no. 48 (2022): 20229616.

12. M. Cui, C. Yang, S. Hwang, et al., "Multi-principal Elemental Intermetallic Nanoparticles Synthesized via a Disorder-to-Order Transition," *Science Advances* 8, no. 4 (2022): eabm4322.

13. Y. S. Yoon, P. Basumatary, M. E. Kilic, et al., "Novel GaPtMnP Alloy Based Anodic Electrocatalyst With Excellent Catalytic Features for Direct Ethanol Fuel Cells," *Advanced Functional Materials* 32, no. 27 (2022): 2111272.

14. M. Bertram, C. Prossl, M. Ronovsky, et al., "Cobalt Oxide-Supported Pt Electrocatalysts: Intimate Correlation Between Particle Size, Electronic Metal-Support Interaction and Stability," *Journal of Physical Chemistry Letters* 11, no. 19 (2020): 8365–8371.

15. Y. Tong, P. Chen, T. Zhou, et al., "A Bifunctional Hybrid Electrocatalyst for Oxygen Reduction and Evolution: Cobalt Oxide Nanoparticles Strongly Coupled to B,N-Decorated Graphene," *Angewandte Chemie International Edition* 56, no. 25 (2017): 7121–7125.

16. Z. Yan, L. Zhao, Y. Liang, et al., "Two-in-one Shell Configurationfor Bimetal Selenides Toward Fast Sodium Storage Withinbroadened Voltage Windows," *Carbon Energy* 4, no. 4 (2022): 586–597.

17. B. P. Vinayan and .R. S. Platinum-TM, "(Co) Alloy Nanoparticles Dispersed Nitrogen Doped (Reduced Graphene Oxide-Multiwalled Carbon Nanotube) Hybrid Structure Cathode Electrocatalysts for High Performance PEMFC Applications," *NanoScale* 5, no. 11 (2013): 5019–5118.

18. M. Melchionna, S. Marchesan, M. Prato, and P. Fornasiero, "Carbon Nanotubes and Catalysis: The Many Facets of a Successful Marriage," *Catalysis Science and Technology* 5, no. 8 (2015): 3859–3875.

19. K. Deng, Y. Xu, D. Yang, et al., "Pt–Ni–P Nanocages With Surface Porosity as Efficient Bifunctional Electrocatalysts for Oxygen Reduction and Methanol Oxidation," *Journal of Materials Chemistry A* 7, no. 16 (2019): 9791–9797.

20. B. You, X. Liu, X. Liu, and Y. Sun, "Efficient H_2 Evolution Coupled With Oxidative Refining of Alcohols via a Hierarchically Porous Nickel Bifunctional Electrocatalyst," *ACS Catalysis* 7, no. 7 (2017): 4564–4570.

21. Y. Ren, C. H. Q. Chang, N. Li, J. Yang, and S. Hu, "Boosting Chemoselective Reduction of 4-nitrostyrene via Photoinduced Energetic Electrons From in Situ Formed Cu Nanoparticles on Carbon Dots," *Green Chemistry* 23, no. 8 (2021): 2938–2943.

22. Y. Tan, X. Y. Liu, L. Li, L. Kang, A. Wang, and T. Zhang, "Effects of Divalent Metal Ions of Hydrotalcites on Catalytic Behavior of Supported Gold Nanocatalysts for Chemoselective Hydrogenation of 3-Nitrostyrene," *Journal of Catalysis* 364 (2018): 174–182.

23. Y. Ji, T. Fan, and Y. Luo, "First-Principles Study on the Mechanism of Photocatalytic Reduction of Nitrobenzene on the Rutile $TiO_2(110)$ Surface," *Physical Chemistry Chemical Physics* 22, no. 3 (2020): 1187.

24. R. Gao, L. Pan, H. Wang, et al., "Breaking Trade-off Between Selectivity and Activity of Nickel-Based Hydrogenation Catalysts by Tuning Both Steric Effect and D-Band Center," *Advancement of Science* 9, no. 10 (2019): 1900054.

25. Y. Sheng, Y. Liu, L. Yin, et al., "Rh Promotional Effects on Pt–Rh Alloy Catalysts for Chemoselective Hydrogenation of Nitrobenzene to p-Aminophenol," *Chemical Engineering Journal* 452 (2023): 139448.

26. Z. Li, X. Dong, S. Ji, et al., "Strong Electronic Interaction of Indium Oxide With Palladium Single Atoms Induced by Quenching Toward Enhanced Hydrogenation of Nitrobenzene," *Applied Catalysis B: Environment and Energy* 313 (2022): 121462.

27. A. Han, J. Zhang, W. Sun, et al., "Isolating Contiguous Pt Atoms and Forming Pt-Zn Intermetallic Nanoparticles to Regulate Selectivity in 4-Nitrophenylacetylene Hydrogenation," *Nature Communications* 10, no. 1 (2019): 3787.

28. J. Guo, F. Feng, S. Zhao, et al., "High FeLS(C) Electrochemicalactivity of an Iron Hexacyanoferrate Cathode Boosts Superiorsodium Ion Storage," *Carbon Energy* 5, no. 5 (2023): 314.

29. J. Zhang, X. Qu, Y. Han, et al., "Engineering PtRu Bimetallic Nanoparticles With Adjustable Alloying Degree for Methanol Electro-Oxidation: Enhanced Catalytic Performance," *Applied Catalysis B: Environmental* 263 (2020): 118345.

30. F. Bao, E. Keppainen, I. Dorbandt, et al., "Understanding the Hydrogen Evolution Reaction Kinetics of Electrodeposited Nickel-Moly-Molybdenum in Acidic, Near-Neutral, and Alkaline Conditions," *ChemElectroChem* 8, no. 1 (2021): 195–208.

31. H. Du, R. M. Kong, X. Guo, F. Qu, and J. Li, "Recent Progress in Transition Metal Phosphides With Enhanced Electrocatalysis for Hydrogen Evolution," *Nanoscale* 10, no. 46 (2018): 21617–21624.

32. M. R. Kandel, U. N. Pan, D. R. Paudel, P. P. Dhakal, N. H. Kim, and J. H. Lee, "Hybridized Bimetallic Phosphides of Ni–Mo, Co–Mo, and Co–Ni in a Single Ultrathin-3D-Nanosheets for Efficient HER and OER in Alkaline media," *Composites Part B: Engineering* 239 (2022): 109992.

33. L. Yu, J. Zhang, Y. Dang, et al., "In Situ Growth of Ni_2P-Cu_3P Bimetallic Phosphide With Bicontinuous Structure on Self-Supported NiCuC Substrate as an Efficient Hydrogen Evolution Reaction Electrocatalyst," *ACS Catalysis* 9, no. 8 (2019): 6919–6928.

34. X. Zhang, A. Wu, D. Wang, et al., "Fine-tune the Electronic Structure in Co-Mo Based Catalysts to Give Easily Coupled HER and OER Catalysts for Effective Water Splitting," *Applied Catalysis B: Environmental* 328 (2023): 122474.

35. C. C. L. McCrory, S. Jung, J. C. Peters, and T. F. Jaramillo, "Benchmarking Heterogeneous Electrocatalysts for the Oxygen Evolution Reaction," *Journal of the American Chemical Society* 135, no. 45 (2013): 16977–16987.

36. A. Manzoor, S. Pandey, D. Chakraborty, S. R. Phillpot, and S. Aidhy, "Entropy Contributions to Phase Stability in Binary Random Solid Solutions," *npj Computational Materials* 4 (2018): 47.

37. Y. F. Ye, Q. Wang, J. Lu, C. T. Liu, and Y. Yang, "High-entropy Alloy: Challenges and Prospects," *Materials Today* 19, no. 6 (2016): 349–362.

38. J. W. Yeh, S. K. Chen, S. J. Lin, et al., "Nanostructured High-entropy Alloys With Multiple Principal Elements: Novel Alloy Design Concepts and Outcomes," *Advanced Engineering Materials* 6, no. 5 (2004): 299.

39. J. D. Chodera and D. L. Mobely, "Entropy-enthalpy Compensation: Role and Ramifications in Biomolecular Ligand Recognition and Design," *Annual Review of Biophysics* 42, no. 1 (2013): 121–142.

40. X. Tang, G. B. Thompson, K. Ma, and C. R. Weinberger, "The Role of Entropy and Enthalpy in High Entropy Carbides," *Computation Materials Science* 210 (2022): 111474.

41. W. Al Zoubi, B. Assfour, A. W. Allaf, S. Leoni, J. H. Kang, and Y. G. Ko, "Experimental and Theoretical Investigation of High-Entropy-Alloy/Support as a Catalyst for Reduction Reactions," *Journal of Energy Chemistry* 81 (2023): 132–142.

42. W. Al Zoubi, R. A. K. Putri, M. R. Abukhadra, and Y. G. Ko, "Recent Experimental and Theoretical Advances in the Design and Science of High-Entropy Alloy Nanoparticles," *Nano Energy* 110 (2023): 108362.

43. Y. Yao, Q. Dong, A. Brozena, et al., "High-Entropy Nanoparticles: Synthesis-Structure-Property Relationships and Data-Driven Discovery," *Science* 376, no. 6589 (2022): 151.

44. W. Al Zoubi, A. Al Mahmud, and F. Hazmathulhaq, "Origin of the Synergistic Effects of Bimetallic Nanoparticles Coupled With a Metal Oxide Heterostructure for Accelerating Catalytic Performance," *SusMat* 4, no. 3 (2024): 216.

45. W. Al Zoubi, S. Leoni, B. Assfor, et al., "Continuous Synthesis of Metal Oxde-supported High-entropy Alloy Nanoparticles With Remarkable Durability and Catalytic Activity in the Hydrogen Reduction," *InfoMat* 7, no. 2 (2025): e212617.

46. W. Al Zoubi, Y. Sheng, I. Hussain, H. Seongjun, and N. Park, "Multi-Principal Element Nanoparticles: Synthesis Strategies and Machine Learning Prediction," *Coordination Chemistry Reviews* 535 (2025): 216656.

47. A. Al Mahmud, A. H. Alshatteri, H. S. Alhasan, et al., "Copper-doped Strontium Metal-organic Frameworks: Dual Function Active Material for Supercapcitor and Oxygen Evolution Reaction," *Electrochimica Act* 503 (2024): 144857.

Supporting Information

Additional supporting information can be found online in the Supporting Information section.

Supporting File 1: sus270029 sup 0001 SuppMat.docx
Supporting File 2: sus270029 sup 0002 SuppMat.docx